Acta Acustica united with Acustica
Vol. 93 (2007) 899 – 908

Computation of Broadband Sound Signal Propagation in a Shallow Water Environment with Sinusoidal Bottom using a 3-D PE Model

Frédéric Sturm
Laboratoire de Mécanique des Fluides et d'Acoustique, UMR CNRS 5509, Centre Acoustique, École Centrale de Lyon, 36, avenue Guy de Collongue, F-69134 Ecully Cedex, France. frederic.sturm@ec-lyon.fr

Summary
In this paper, numerical results of sound propagation in a three-dimensional oceanic waveguide with a sinusoidal (corrugated) bottom are reported. A broadband sound pulse with a center frequency of 25 Hz and a bandwith of 30 Hz is considered. This acoustic problem was previously studied by Collins and Chin-Bing considering a harmonic point source [J. Acoust. Soc. Am. **87**(3), 1104-1109 (1990)]. The numerical method used to solve the 4-D acoustic problem is based on a Fourier synthesis of frequency-domain solutions. The calculations in 3-D are carried out using the fully 3-D parabolic equation based model 3DWAPE. To analyze the acoustic problem, we follow closely the methodology used in previous works to investigate the 3-D ASA wedge and 3-D Gaussian canyon benchmarks [F. Sturm, J. Acoust. Soc. Am., **117**(3), 1058-1079 (2005)]. Results corresponding to a 25 Hz continuous wave point source are first presented and compared with predictions by another model. Then, the acoustic problem is solved considering the broadband source pulse. The modal structure of the received signals on several distinct vertical arrays is analyzed and clearly exhibits mode arrivals of the propagating signal not predicted by pseudo-3-D or 2-D PE models.

PACS no. 43.30.Bp, 43.30.Dr, 43.30.Gv

1. Introduction

Over the last few decades, abundant literature on the propagation of acoustic waves in three-dimensional (3-D) oceanic waveguides has been published. The reader is referred to [1] for a detailed review of the main 3-D models used by the underwater acoustics community. In an effort to benchmark 3-D propagation models, several test cases were considered by modelers. Most of them include an idealized bottom geometry such as a conical seamount [2, 3, 4, 5], a ridge [6], a wedge-shaped waveguide [7, 8, 9, 10, 11, 12, 13, 14, 15], and a Gaussian canyon [16, 17].

In this paper, numerical results of sound propagation in a three-dimensional oceanic waveguide with a sinusoidal (corrugated) bottom are reported. This acoustic problem was first proposed by Collins and Chin-Bing [18] for a harmonic point source emitting at a very low frequency (25 Hz): The 3-D solutions were computed using a 3-D parabolic equation (PE) based model. Here, a broadband sound pulse with a center frequency of 25 Hz and a bandwith of 30 Hz is considered. In the original paper of Collins and Chin-Bing, the 3-D PE results were shown for a maximum propagation range equal to 12 km. The 3-D effects were consistent with those predicted by ray tracing. Note that the rays were traced with a maximum propagation range equal to 50 km, showing more pronounced 3-D effects than in the first 12 km. In the present work, the original maximum propagation range is multiplied by three. The numerical method used to solve the 4-D acoustic problem is based on a Fourier synthesis of frequency-domain solutions. The calculations in 3-D are carried out using the fully 3-D parabolic equation based model 3DWAPE [19, 15, 17]. To analyze the acoustic problem, we follow closely the methodology used in previous works to investigate the 3-D ASA wedge and the 3-D Gaussian canyon [17].

The paper is organized as follows: In the next section, the shallow water acoustical problem is described. In Sec. 3, the 3-D PE results corresponding to a 25 Hz continuous wave (CW) point source are presented and CPU times are given. The modal structure of the 3-D field is analyzed and the 3-D effects are compared with those predicted by adiabatic modal theory. Then, the acoustic problem is solved in 4-D considering the broadband source pulse. The time signals received by two sets of vertical arrays placed along the channel axis are presented. The modal structures of the received signals clearly exhibit mode arrivals of the propagating signal not predicted by pseudo-3-D or 2-D PE models. The paper closes with a brief section of concluding remarks.

Received 25 January 2007, revised 11 July 2007,
accepted 28 July 2007.

2. Description of the 3-D test case

An isotropic point source S is placed at a depth $z_S = 25$ m in an environment consisting of a lossless homogeneous water layer overlying a lossy half-space fluid sediment bottom. The water layer has a sound speed of 1500 m/s and a density of 1 g/cm^3. The bottom has a sound speed, a density and an absorption of 1700 m/s, 1.5 g/cm^3, and 0.5 dB/wavelength respectively, which leads to a critical grazing angle of approximately 28°. No shear energy is assumed in the sediment. The geometry of the corrugated bottom is depicted in Figure 1. Using cylindrical coordinates, with z the depth (increasing downwards) below the ocean surface, θ the azimuthal (bearing) angle, and r the horizontal range from the source, the water/sediment interface is described by the surface $\{z = h(r,\theta)\}$ where

$$h(r,\theta) = 150 - 50 \sin\left(\frac{2\pi r \cos\theta}{6000}\right). \qquad (1)$$

Let x and y denote the two horizontal Cartesian coordinates related to r and θ by $x = r\cos\theta$ and $y = r\sin\theta$. The water depth only varies in the x direction. For the particular azimuthal angles $\theta = 0°$ and $\theta = 180°$ (*i.e.* along the positive and negative x axis), the water/sediment interface is a sinusoid of 6000-m periodicity, the minimum and maximum water depths being, respectively, 100 m and 200 m. The water depth at the source location is 150 m. The bottom slope depends on r and θ. For instance, at the source (*i.e.* at $r = 0$), the bottom is upsloping for $\theta = 0°$ and downsloping for $\theta = 180°$. The bottom is flat for $\theta = 90°$ and $\theta = 270°$ (*i.e.* along the positive and negative y axis). Notice that the $\theta = 0°$ azimuthal angle has been chosen to be aligned with the direction with maximum slope ($\approx 2.99°$) at initial range.

The time-dependence of the source is a Gaussian-weighted cosine pulse (with center frequency $f_c = 25$ Hz) given by

$$S(t) = \cos\left(2\pi f_c t\right) \exp\left[-(5\pi t)^2\right]. \qquad (2)$$

Due to the geometry of the corrugated bottom, we expect relatively large 3-D effects in the vicinity of $\theta = 90°$ and at large ranges. We thus position a network of vertical arrays along six azimuthal angles (90°, 92°, 94°, 96°, 98°, 100°) and at two ranges from the point source: 20 km (vertical arrays labelled A1–A6) and 30 km (vertical arrays labelled B1–B6). Each vertical array is composed of 20 elements evenly spaced in depth between 10 m and 200 m. It should be noted that the number of elements present in the water column can vary from one vertical array to another.

All the numerical simulations shown in the next sections were performed on a 2.8-GHz mono-processor workstation with a 2-GB memory. Neither vectorization nor parallel computing was used. Unless specified otherwise, all the following numerical results were obtained using the 3-D PE model 3DWAPE.

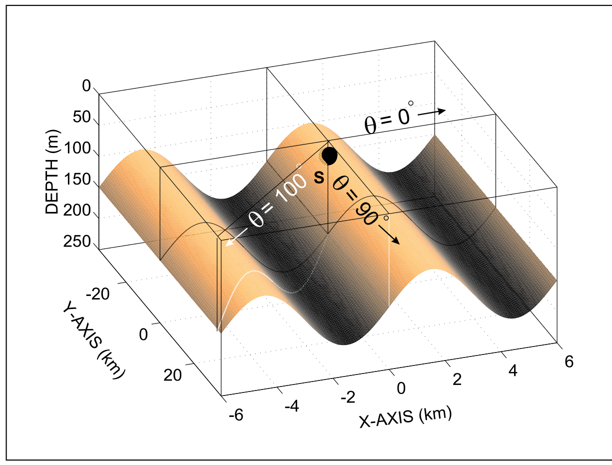

Figure 1. Geometry of the sinusoidal waveguide.

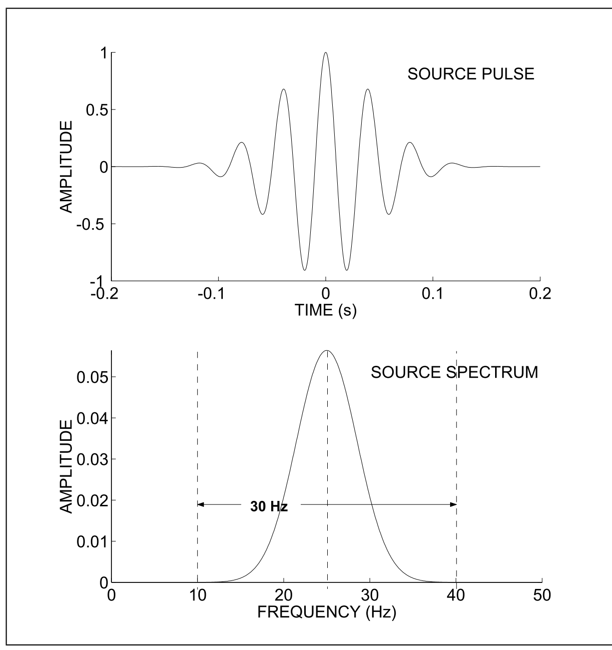

Figure 2. Time-dependence of the source pulse (upper subplot) and its spectrum (lower subplot).

3. Analysis of the acoustical problem at 25 Hz

The source pulse being centered at 25 Hz, we analyze first the acoustic problem at that specific frequency. Due to the weak dependence of the medium characteristics on r, the propagating field is expected to be dominated by its outgoing component (*i.e.* backscattering energy is negligible) and to have small angles of propagation with respect to the horizontal. As we are mainly interested in long range propagation and assuming that r^{-2} approximately commutes with $\partial/\partial r$ for $r \gg 0$, the (elliptic-type) boundary value

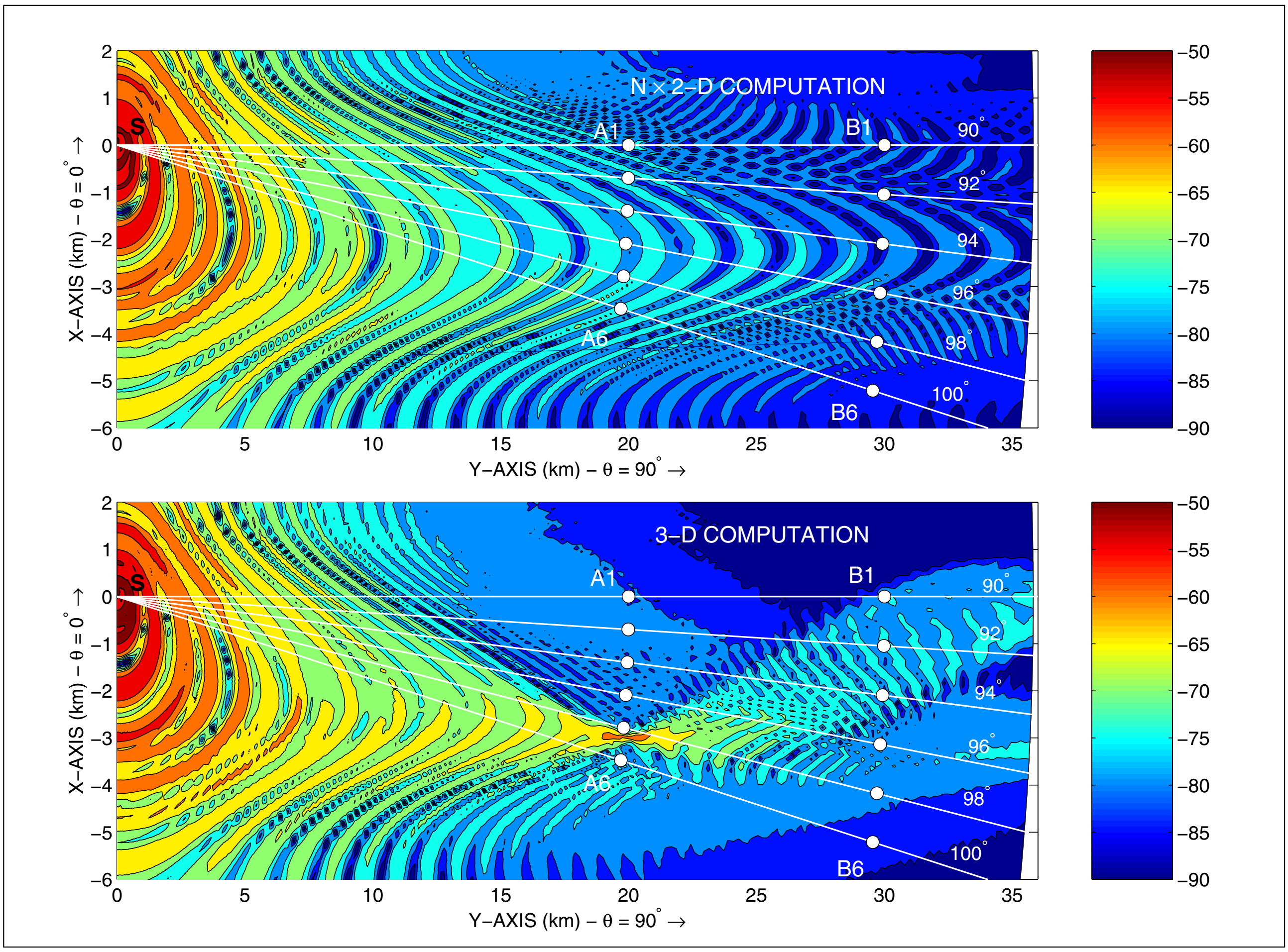

Figure 3. Horizontal slices (at a constant depth of 30 m) of the transmission loss (in dB re 1 m) corresponding to N×2-D (upper subplot) and 3-D (lower subplot) PE calculations.

problem based on the 3-D Helmholtz equation is replaced by the following initial- and boundary-value problem

$$\begin{cases} \dfrac{\partial \psi}{\partial r} = \mathrm{i}k_0 \left(\displaystyle\sum_{k=1}^{n_\mathrm{p}} \frac{a_{k,n_\mathrm{p}} \mathcal{X}}{\mathcal{I} + b_{k,n_\mathrm{p}} \mathcal{X}} + \frac{\frac{1}{2}\mathcal{Y}}{\mathcal{I} + \frac{1}{4}\mathcal{Y}} \right) \psi, \\ \psi(r_0, \theta, z; \omega_\mathrm{c}) = \psi^{(0)}(\theta, z; \omega_\mathrm{c}), \end{cases} \tag{3}$$

where $\psi = \psi(r, \theta, z; \omega_\mathrm{c})$ represents the acoustic field for $r_0 \le r \le r_\mathrm{max}$, $0 \le \theta \le 2\pi$, $0 \le z \le z_\mathrm{max}$, and is related to the acoustic pressure field $\widehat{P} = \widehat{P}(r, \theta, z; \omega_\mathrm{c})$ by

$$\widehat{P}(r, \theta, z; \omega_\mathrm{c}) = H_0^{(1)}(k_0 r)\, \psi(r, \theta, z; \omega_\mathrm{c}), \tag{4}$$

where $H_0^{(1)}$ represents the zeroth-order Hankel function of the first kind, and $k_0 = \omega_\mathrm{c}/c_0$ with c_0 a reference sound speed. In Eq. (3), n_p is the number of Padé terms, a_{k,n_p}, b_{k,n_p}, $1 \le k \le n_\mathrm{p}$, are the complex- or real-valued Padé coefficients [20], and $\psi^{(0)}$ denotes the initial outgoing field simulating a point source at $r = 0$ and $z = z_S$. Here, $\mathcal{I}$ is the identity operator, $\mathcal{X}$ is the 2-D depth operator in the rz-plane defined by

$$\mathcal{X} = \left(n_\alpha^2(r, \theta, z) - 1 \right) \mathcal{I} + \frac{\rho}{k_0^2} \frac{\partial}{\partial z} \left(\frac{1}{\rho} \frac{\partial}{\partial z} \right), \tag{5}$$

with $n_\alpha = (c_0/c(r, \theta, z))(1 + \mathrm{i}\eta\alpha)$, α the attenuation coefficient expressed in dB per wavelength, and $\eta = 1/(40\pi \log_{10} \mathrm{e})$. The azimuthal operator $\mathcal{Y}$ is defined by

$$\mathcal{Y} = \frac{1}{(k_0 r)^2} \frac{\partial^2}{\partial \theta^2}. \tag{6}$$

Neglecting $\mathcal{Y}$ but retaining the azimuthal dependence in $n_\alpha(r, \theta, z)$ would lead to a N×2-D PE model which could not predict horizontal refraction of the propagating energy. Note that a N×2-D model is also referred to as a pseudo-3-D model in the literature. The Padé series expansion present in the parabolic equation allows for a very-wide-angle propagation in depth *via* a meticulous selection of parameter n_p. The [1/1] Padé-like rational-function approximation used for the azimuthal operator $\mathcal{Y}$ can be seen as an azimuthal quadratic correction of the original linear parabolic equation derived by Tappert [21]. The 3-D PE model has thus a wide-angle capability in both depth and azimuth separately, but cannot be properly considered as having a wide-angle capability in all directions, due to the coupling of the operators $\mathcal{X}$ and $\mathcal{Y}$ in the residual of the Padé approximation of $\sqrt{\mathcal{I} + \mathcal{X} + \mathcal{Y}}$ in (3), as is explained in the discussion in [17].

Calculations were carried out using a 10-m range step and a 1-m depth step (*i.e.,* $\Delta r = \lambda/6$ and $\Delta z = \lambda/60$ where λ denotes the acoustic wavelength), a Padé-2 approximation in depth ($n_\mathrm{p} = 2$) and a reference sound speed $c_0 = 1500$ m/s. The maximum depth of the computational grid was equal to 600 m. The 3-D solution was obtained using 4680 azimuthal points with a 8th-order FD scheme in azimuth, which corresponds, at the maximum computation range, to an arclength increment ΔS between adjacent angles of approximately $4\lambda/5$. The advantages and drawbacks of using high-order FD scheme to handle the azimuthal derivative term were thoroughly discussed in [15]. Note however that the use of a more classical second-order FD azimuthal scheme would require $\Delta S \approx \lambda/10$ at the maximum computation range, and hence, approximately 37800 points would be needed in azimuth. Due to the geometrical symmetry of the acoustical problem about the $\theta = 0°$ azimuth, only $2341 = (4680/2) + 1$ points were used in the 3-D computation. The 2-D and 3-D marching PE algorithms were initialized at $r_0 = 10$ m using the following source:

$$\psi^{(0)}(\theta, z; \omega_\mathrm{c}) = \sqrt{r_0}\, \mathrm{e}^{-\mathrm{i}(k_0 r_0 - \frac{\pi}{4})} \left[\frac{\mathrm{e}^{\mathrm{i}k_0 R_0^-}}{R_0^-} - \frac{\mathrm{e}^{\mathrm{i}k_0 R_0^+}}{R_0^+} \right], \tag{7}$$

where $R_0^\pm = \sqrt{r_0^2 + (z \pm z_S)^2}$. The source is thus omnidirectional. The 3-D calculation took 40 mn 24 s of CPU time. For comparison, the N×2-D calculation using the same number of points in azimuth took 29 mn 2 s. Of course, it is not necessary to use such a large number of points in azimuth when processing N×2-D computation and, usually, 360 points in azimuth are sufficient to re-construct a horizontal plot of the N×2-D field. For the present test case, a N×2-D run using 360 points in azimuth took 2 mn 13 s.

Horizontal slices of the transmission loss (TL $= -20 \cdot \log_{10}(|\psi(r, \theta, z; \omega_\mathrm{c})|)/\sqrt{r}$) are shown in Figure 3 for the N×2-D (upper subplot) and 3-D (lower subplot) solutions. They correspond to a receiver depth of 30 m. The positions of both the point source and the two sets of receiver arrays are indicated on each subplot. The N×2-D solution displayed in the upper subplot of Figure 3 was obtained by first performing independently 2-D PE computations in adjacent vertical planes centered on the source and then, once this first step accomplished, by re-constructing a 3-D picture of the acoustic field. It should be noted that the bottom slope being different from one vertical plane to another, the N×2-D solution exhibits a θ-dependence of the acoustic field. By comparing the N×2-D and 3-D solutions in Figure 3, one can observe that the main 3-D effects are located along the channel axis and at long ranges. These 3-D effects can be easily explained by the fact that during its propagation, the acoustical energy is horizontally refracted by the sidewalls of the sinusoidal bottom, consequently trapped in the deeper part of the waveguide, and channeled in the y direction.

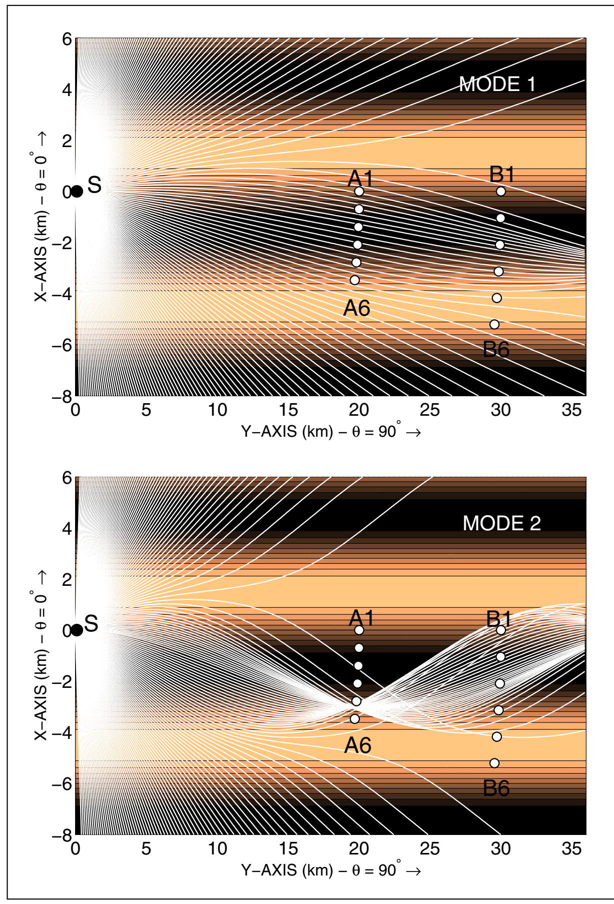

Figure 4. Modal ray diagrams (top view) for the first (upper subplot) and second (lower subplot) modes excited omnidirectionally at the source position for a 25 Hz source.

To better understand the horizontal coupling effects present in the waveguide, we display in Figure 4 the modal ray diagrams in the xy horizontal plane corresponding to each of the propagating modes. Recall that the water depth is equal to 150 m at the source location. Therefore, an harmonic point source emitting at a frequency of 25 Hz leads to only 2 propagating modes. The derivation of the modal ray paths is based on adiabatic modal theory [7]. The modal-ray paths were calculated using closely the method given in [11]. The effects of the 3-D sinusoidal bathymetry on the modal propagations are evident. The 3-D effects are more pronounced for mode 2 than for mode 1. Though clearly present at one ridge of the corrugated bottom, no well-marked shadow zone is observed for mode 1 for $r \leq 36$ km along the channel axis. Anticipating the analysis of broadband results (see Sec. 4), one can predict time arrivals of mode 1 at all receiver arrays A1–A6 and B1–B6. Pursuing the 3-D computation further in range would certainly allow us to capture the shadow zone associated to mode 1 along the $\theta = 90°$ azimuthal direction. It should be noted that there is only one single modal ray associated to mode 1 at each receiver array. Hence, we expect only one single time arrival of the signal carried by mode 1 on arrays A1 – A6, B1 – B6. For mode 2, the situation is more complex. Unlike mode 1, the mode-2 ray paths show a prominent shadow zone region (starting at approximately 15 km and ending around 28 km along the $\theta = 90°$ direction) and also a caustic (around 20 km in the vicinity of the $\theta = 98°$ direction). Again, anticipating the broadband analysis of Sec. 4, one can predict no (or very weak) time arrivals associated to mode 2 at some receiver arrays (*e.g.* A1 or A2) and time arrivals with high intensity at others (*e.g.* A5 or A6). We note that there are regions with multiple mode-2 ray paths. We thus expect to have multiple time arrivals of the signal carried by mode 2 at some receiver arrays (*e.g.* B1 or B3).

The above analysis of the acoustical problem using a modal ray approach helps us in analyzing the 3-D effects observed along specific azimuths. Vertical slices of the transmission loss for selected azimuths are displayed in Figure 5 ($\theta = 90°$), Figure 6 ($\theta = 94°$), and Figure 7 ($\theta = 100°$). For each of the three azimuths considered, both 2-D and 3-D PE solutions are displayed. Let us compare first the 2-D and 3-D solutions along the $\theta = 90°$ vertical direction (see Figure 5). After a few kilometers from the source, the differences between the 2-D and 3-D solutions become more and more pronounced as r increases. Recall that only two propagating modes are excited at the source, and that, along the $\theta = 90°$ azimuth, the water depth has a constant value of 150 m. The 2-D field exhibits for all ranges the interference pattern of the two propagating modes initially present at the source. On the contrary, the interference pattern of the 3-D field is modified during the propagation, due to the horizontal refraction effects of each propagating mode. For ranges approximately less than 15 km, the two (initially present at the source) propagating modes are still there. Then, due to the three-dimensional shadowing effect of mode 2, the influence of mode 2 in the interference pattern progressively disappears, leading to only one propagating mode for r greater than 15 km (approximately) until a distance of $\approx$ 29 km at which mode 2 re-appears. These 3-D effects are consistent with those predicted using adiabatic modal ray theory.

Let us focus now on the acoustic field along $\theta = 94°$ (see Figure 6) and $\theta = 100°$ (see Figure 7). Again, we observe that the 2-D and 3-D solutions, though similar at short range, differ a lot at longer ranges. The 3-D effects experienced by mode 2 are clearly distinguishable. For instance, for $\theta = 94°$, due to out-of-plane propagation, mode 2 disappears at $r \approx 15$ km, re-appears at $r \approx 24$ km, and progressively re-disappears at $r \approx 32$ km. Again, this is consistent with the modal ray diagrams associated to mode 2. Unlike what has been observed for $\theta = 90°$, the differences between the 2-D and 3-D solutions along these two distinct azimuths cannot be attributed to mode 1 and mode 2 only. Indeed, for θ varying from 90° to 270°, a downsloping bottom is first encountered. As a consequence, part of the continuous modal spectrum can be coupled into the propagating spectrum and more than two propagating modes can exist in the deeper part of the waveguide. A water depth of 200 m supports three propagating modes, and, indeed, we clearly notice in the 2-D field shown in the upper subplot of Figure 7 (corresponding to $\theta = 100°$) the presence of three propagating modes for the 200-m water depth at $r \approx 9$ km. Only two modes are present at the same range and azimuthal angle in the 3-D field (shown in the lower subplot of Figure 7). Therefore, the 3-D effects detected by the 3-D PE computation cannot be only attributed to the two propagating modes present at the source location. The 3-D effects undergone by the additional propagating modes cannot be modeled by the adiabatic modal ray approach. Hence, to

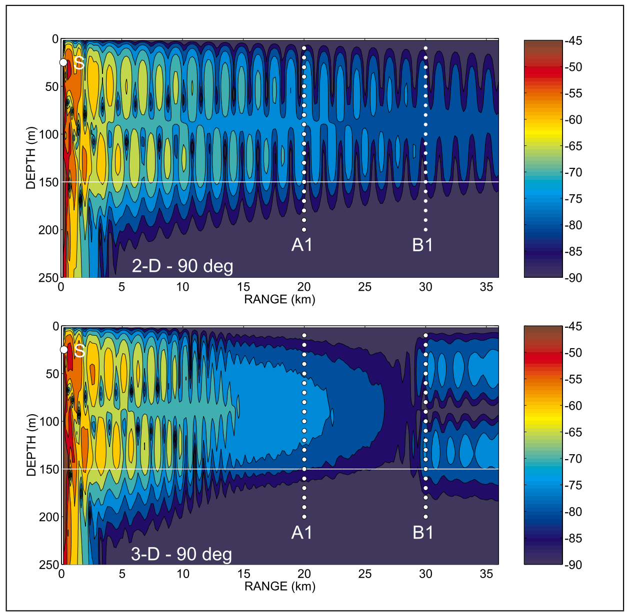

Figure 5. Vertical slices (at constant azimuth $\theta = 90°$) of transmission loss (in dB re 1 m) at 25 Hz corresponding to N×2-D (upper subplot) and 3-D (lower subplot) PE calculations.

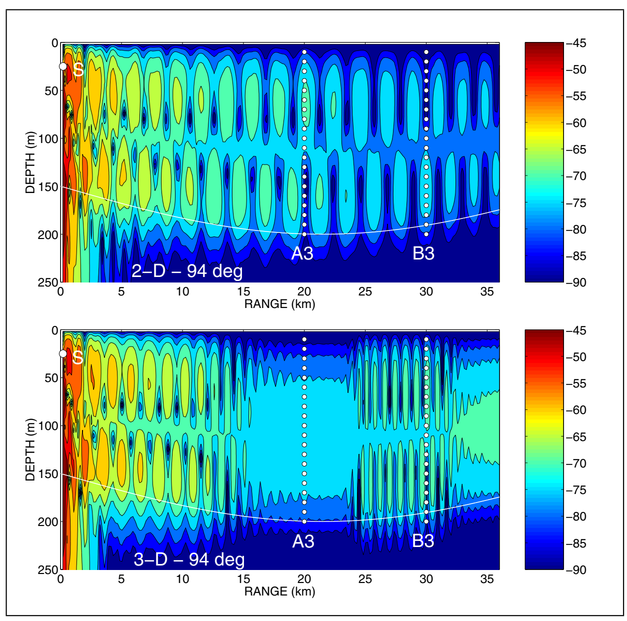

Figure 6. Vertical slices (at constant azimuth $\theta = 94°$) of transmission loss (in dB re 1 m) at 25 Hz corresponding to N×2-D (upper subplot) and 3-D (lower subplot) PE calculations.

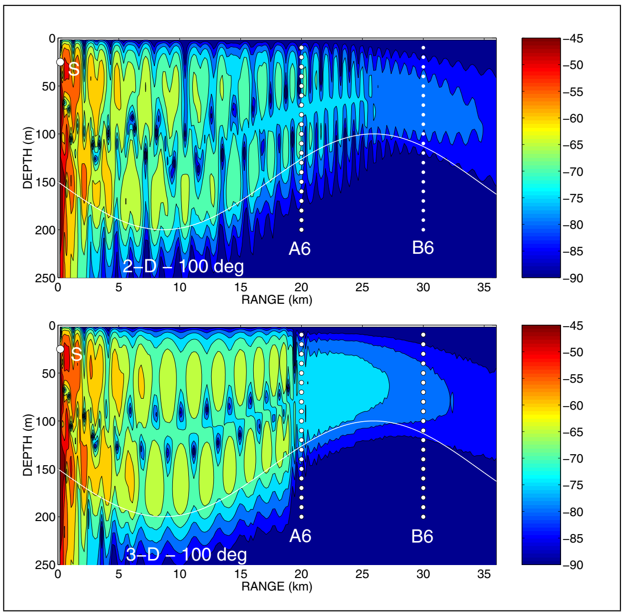

Figure 7. Vertical slices (at constant azimuth $\theta = 100°$) of transmission loss (in dB re 1 m) at 25 Hz corresponding to N×2-D (upper subplot) and 3-D (lower subplot) PE calculations.

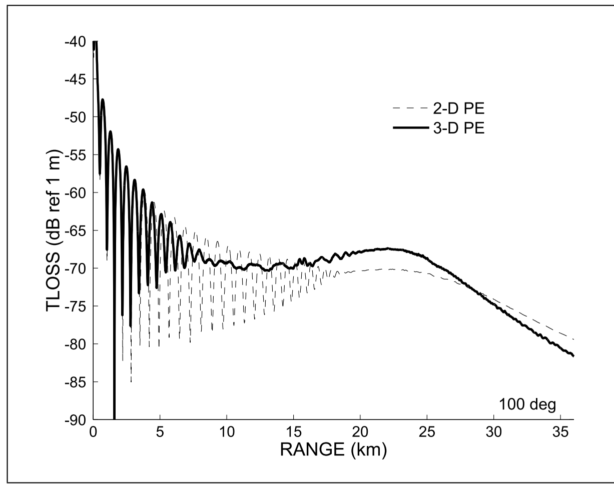

Figure 8. 2-D and 3-D transmission loss comparison at a receiver depth of 30 m and along the 100° azimuth. The thin dashed curve is a 2-D PE calculation and the bold solid curve is a 3-D PE calculation. The source S is placed at a depth $z_S = 89$ m.

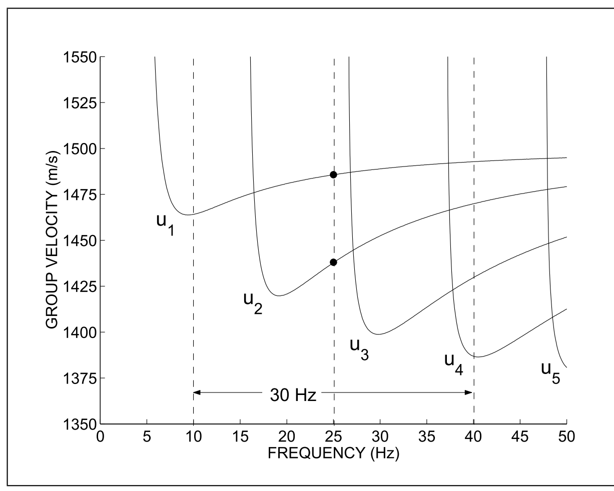

Figure 9. Frequency dependence of group velocities for the first modes corresponding to a 150-m deep Pekeris waveguide.

identify them, we have displaced the point source to a depth of 89 m. This new immersion corresponds to a null of the shape function associated to mode 2. Curves of TL-versus-range at a depth of 30 m and along $\theta = 100°$ are plotted in Figure 8. Mode 2 being poorly excited, the 2-D solution shows the interferences of mode 1 and mode 3 for ranges corresponding to the deeper part of the waveguide along that azimuthal direction. Note that after $r \approx 18$ km, mode 3 has disappeared due to well-known cutoff phenomema during upslope propagation. Similarly, the 3-D solution shows the interferences of mode 1 and mode 3 but we observe that the cutoff of mode 3 appears at a shorter range (approximately 8 km). As an evidence, this cutoff of mode 3 is due to out-of-plane propagation and not upslope propagation.

4. Broadband results

We consider now the broadband source pulse given in Eq. (2). The pulse response at a specific receiver located at range r, azimuth θ, and depth z, is obtained via a Fourier transform of the frequency-domain solution using

$$P(r,\theta,z;t) = \frac{1}{2\pi}\int_{-\infty}^{+\infty} \widehat{S}(\omega) H_0^{(1)}(k_0 r)\psi(r,\theta,z;\omega)\mathrm{e}^{-\mathrm{i}\omega t}\,\mathrm{d}\omega,$$

where $\psi = \psi(r,\theta,z;\omega)$ is the solution of the frequency-domain parabolic equation given in (3), and where $\widehat{S}(\omega)$ is the source spectrum given by

$$\widehat{S}(\omega) = \int_{-\infty}^{+\infty} S(t)\,\mathrm{e}^{\mathrm{i}\omega t}\,\mathrm{d}t.$$

The frequency integrals are evaluated numerically using a Discrete Fourier transform (DFT). Note that the amplitude of the source spectrum is neglectable for frequencies below 10 Hz and above 40 Hz (see Figure 2).

In the simulations, we considered a bandwidth of 30 Hz, thus covering the band 10 − 40 Hz. A time window of length $T = 12$ s, with 4096 points, was used in the DFT algorithm, yielding values of the received signals with a very fine time resolution $\Delta t \approx 0.0029$ s compared to the total length of the source signal. The length of the time window corresponds to a frequency sampling $\Delta f \approx 0.0833$ Hz, and leads to 361 discrete values within the frequency-band of interest. Both 2-D and 3-D PE calculations were carried out using a frequency-dependent range step and depth step of $\lambda/10$ and $\lambda/60$ respectively. Similarly, the number of points in the azimuthal direction used when performing 3-D calculations was dependent on frequency. It was equal to 2160 at 10 Hz and 7560 at 40 Hz. A linear interpolation between these two extreme values was used for the other

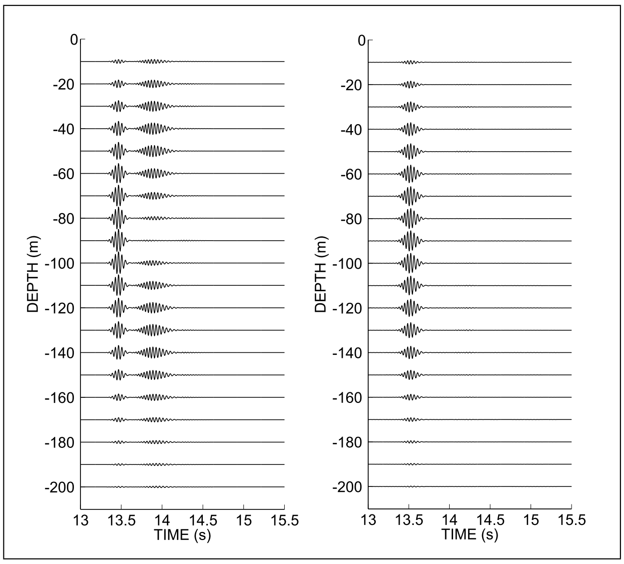

Figure 10. Stacked time series versus depth corresponding to vertical array A1 (placed at 20 km along the azimuth $\theta = 90°$) obtained using 2-D (left) and 3-D (right) computations.

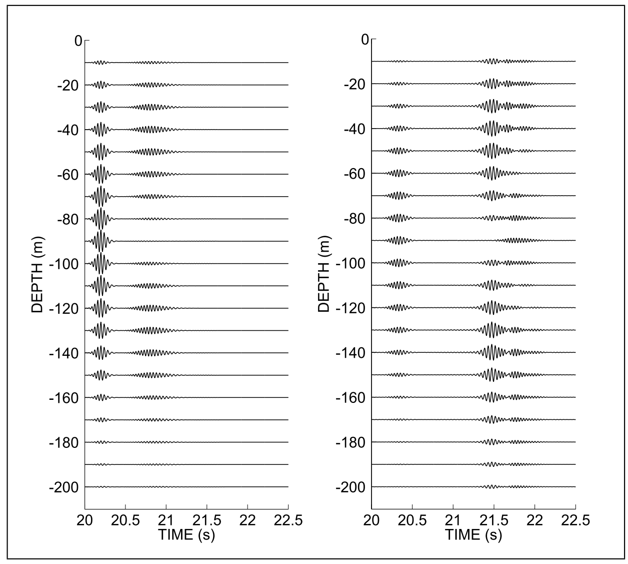

Figure 12. Stacked time series versus depth corresponding to vertical array B1 (placed at 30 km along the azimuth $\theta = 90°$) obtained using 2-D (left) and 3-D (right) computations.

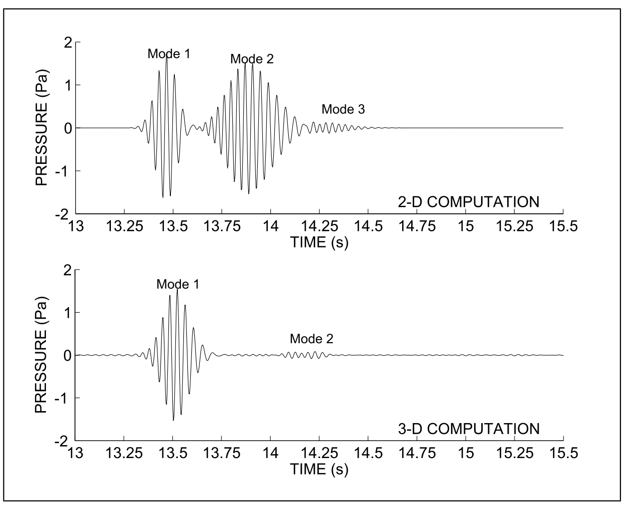

Figure 11. Signal received on vertical array A1 (r = 20 km, θ = 90°) at a depth of 30 m obtained using 2-D (upper subplot) and 3-D (lower subplot) computations.

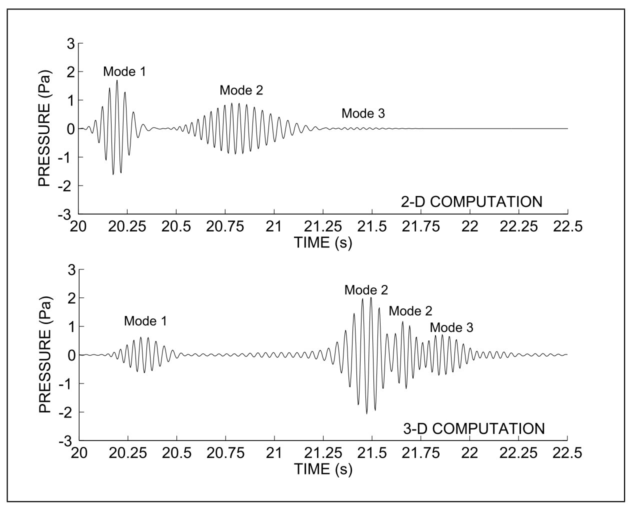

Figure 13. Signal received on vertical array B1 (r = 30 km, θ = 90°) at a depth of 30 m obtained using 2-D (upper subplot) and 3-D (lower subplot) computations.

discrete frequencies within the band 10 – 40 Hz. For each frequency computation, both 2-D and 3-D PE algorithms were initialized using the field given by Eq. (7). As for the 25 Hz CW source, a Padé-2 approximation was used in depth. The 3-D calculation took 13 days 20 hours 25 minutes of CPU time. For comparison, the 2-D calculation only took 26 mn 37 s.

Let us analyze first the time signals received on vertical arrays A1 and B1 positioned in the same 150-m isobath vertical plane ($\theta = 90°$) at two distinct ranges 20 km and 30 km respectively. The computed dispersion curves (corresponding to a 150-m water depth) for the first 5 propagating modes are shown in Figure 9. They confirm the existence of only 2 propagating modes for a CW point source emitting at 25 Hz. Note that the center frequency is below the cutoff frequency of mode 3. This suggests that mode 3 be very weak at both vertical arrays A1 and B1. The pulses received on A1 are displayed in Figure 10. They were obtained using 3-D computations. In particular, the signal received on A1 at a depth of 30 m is plotted in Figure 11. Similarly, the time signals received on B1 are displayed in Figure 12 and the signal received at z = 30 m is plotted in Figure 13. Both 2-D and 3-D solutions were multiplied by a factor r to compensate for spherical spreading. For comparison, the signals obtained using 2-D computation are systematically displayed. As expected, the 2-D pulses received on A1 and B1 are both composed of two successive wave packets which can be unambiguously attributed to mode 1 and mode 2, followed by a weak wave packet attributed to mode 3. The modal arrivals are more dispersed at 30 km than at 20 km and the mode-3 wave packet is nearly undistinguishable at 30 km. Looking now at the

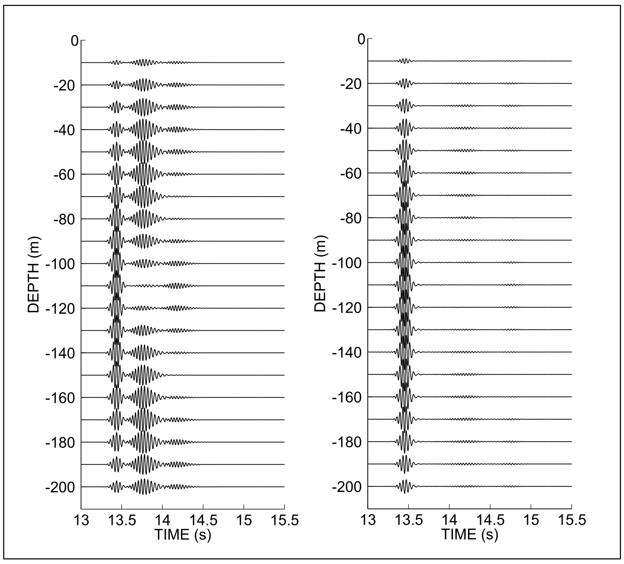

Figure 14. Stacked time series versus depth corresponding to vertical array A3 (placed at 20 km along the azimuth $\theta = 94°$) obtained using 2-D (left) and 3-D (right) computations.

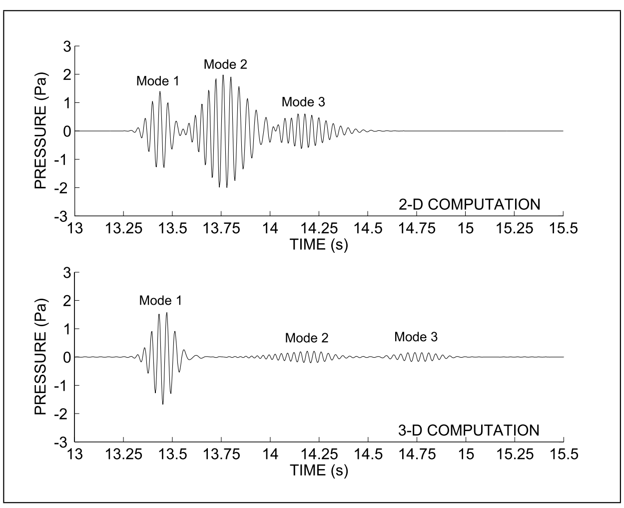

Figure 15. Signal received on vertical array A3 ($r = 20$ km, $\theta = 94°$) at a depth of 30 m obtained using 2-D (upper subplot) and 3-D (lower subplot) computations.

3-D solution, the pulses received on A1 consist mainly of one single wave packet (mode 1), with a slight shift in time and more dispersed than the corresponding 2-D mode-1 wave packet. This is due to the fact that, though weaker than those of mode 2, the 3-D effects experienced by mode 1 are yet present. One can observe also a very weak time arrival centered around $t = 14.2$ s (visible in the lower subplot of Figure 11). By increasing its amplitude for all depths (not shown here), one can show that this second wave packet corresponds to a time arrival of mode 2 (not predicted by adiabatic modal ray theory). The 3-D pulses received on B1 are composed of four successive wave packets. The first one is well separated from the three others. It corresponds to a time arrival of mode 1. Note that due to out-of-plane propagation, this first wave packet is different from the corresponding 2-D first wave packet. The second and third wave packets correspond to two distincts (but very close) mode-2 time arrivals. The fourth packet corresponds to mode 3, its amplitude being of the same order as that of mode 1.

The pulses received on vertical array A3 ($r = 20$ km, $\theta = 94°$) are displayed in Figure 14 and the signal received on A3 at a depth of 30 m is plotted in Figure 15. Again, the corresponding 2-D pulses are plotted for comparison. The water depth is close to 200 m at A3 and supports three propagating modes at 25 Hz. Accordingly, the 2-D received signals consist of three successive wave packets centered at $t = 13.45$ s, $t = 13.75$ s, $t = 14.15$ s, respectively, and associated to the three propagating modes. The 3-D pulses received on A3 consist mainly of one single wave packet (mode 1) centered around $t = 13.45$ s, followed by two weak packets, the first one corresponding to mode 2 centered at $t = 14.2$ s, and the second one to mode 3 centered at $t = 14.75$ s.

The signal arrivals on the six vertical arrays A1 – A6 obtained using 3-D computation are displayed in Figure 16. Note that the signals plotted in the first and third panels of Figure 16 correspond to the ones shown in the right subplots of Figures 10 and 14 respectively. As expected, due to the weak horizontal refraction of the first propagating mode, we observe the presence of mode 1 at each vertical array. On the contrary, due to the more pronounced 3-D effects of the second propagating mode, moving from $\theta = 90°$ to $\theta = 100°$, we see that mode 2 is nearly absent of the first vertical arrays and progressively appears until $\theta = 98°$ (array A5) where its amplitude reaches its maximum. This is consistent with the observations made on the mode-2 ray diagrams in the previous section. The signals received on the six vertical arrays B1 – B6 obtained using 3-D computation are displayed in Figure 17. The signals plotted in the first panel of Figure 17 correspond to the ones shown in the right subplot of Figure 12. Again, mode 1 is present at each vertical array. We now observe the presence of mode 2 at the first vertical arrrays. The long mode-2 wave packet observed at $\theta = 94°$ correspond to the merger of multiple arrivals of mode 2.

5. Concluding remarks

In summary, the propagation of a broadband sound pulse in a three-dimensional oceanic waveguide with a sinusoidal bottom was investigated numerically in this paper. The approach chosen to analyze this 4-D acoustical problem was deliberately similar to the methodology followed in [17]. First, the problem was studied considering a CW point source emitting at the center frequency (25 Hz). For mode 1 and mode 2, the horizontal refraction effects predicted by the adiabatic-modal ray theory agreed satisfactorily with those predicted by 3-D PE computations. However, by changing the depth of the source, it became obvious that the 3-D effects could not be attributed only to the two propagating modes present at the source location. Then, the time signals received by a set of vertical arrays positioned along the channel axis were computed.

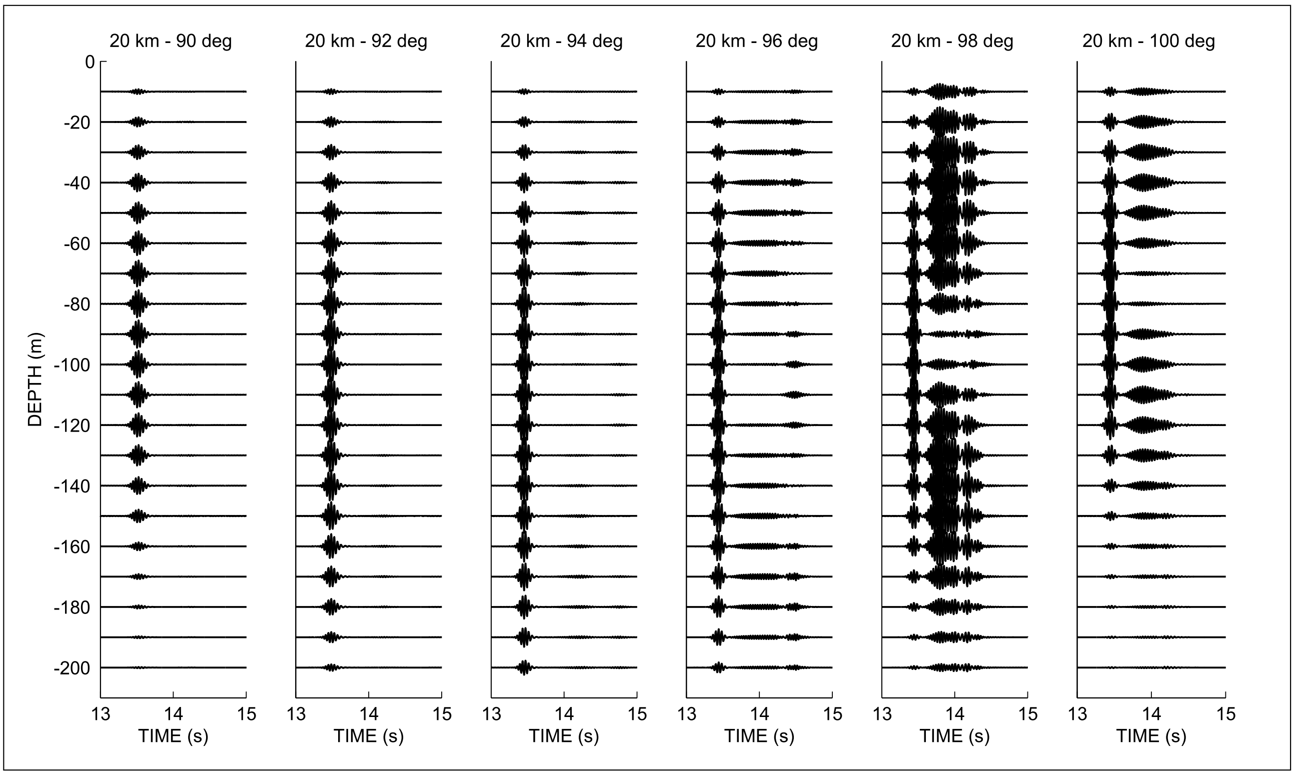

Figure 16. Stacked time series vs depth corresponding to A1 – A6 (placed at 20 km along the azimuths 90°, 92°, 94°, 96°, 98°, 100°) obtained using 3-D computation.

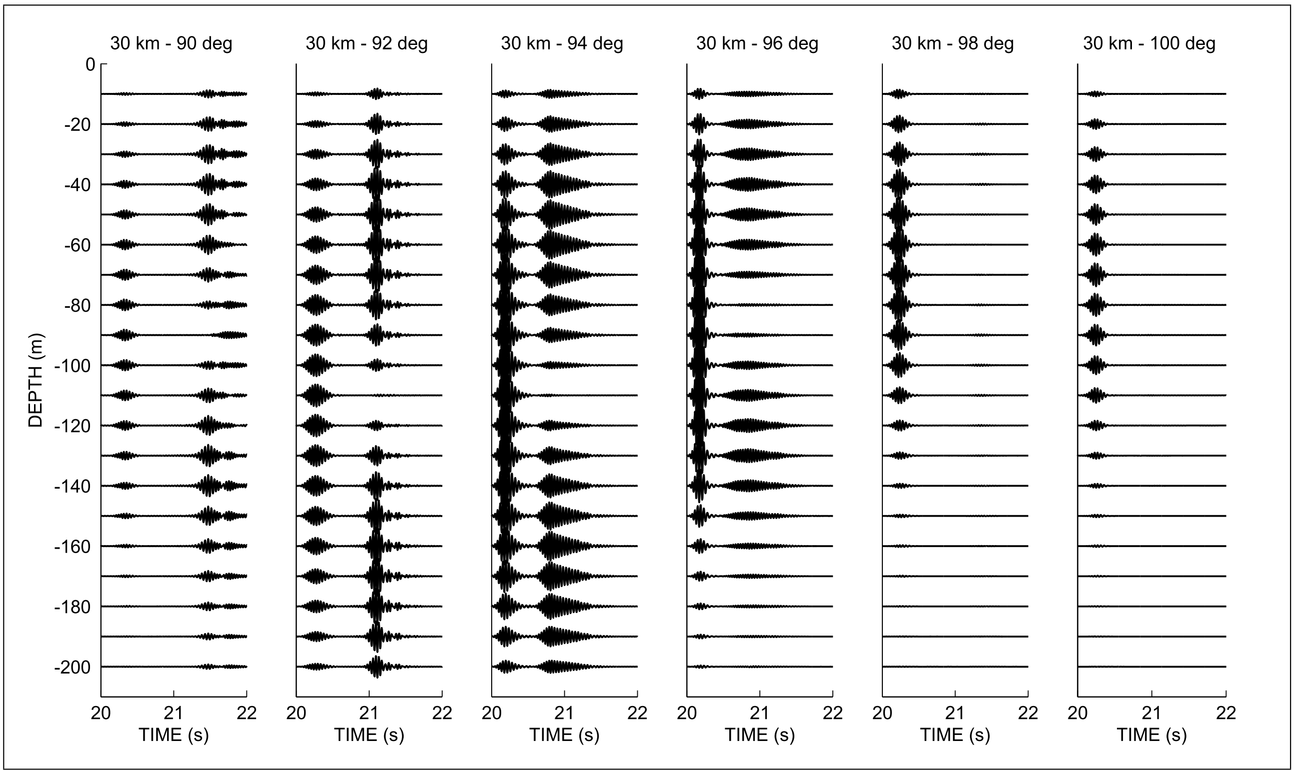

Figure 17. Stacked time series vs depth corresponding to B1 – B6 (placed at 30 km along the azimuths 90°, 92°, 94°, 96°, 98°, 100°) obtained using 3-D computation.

The time series exhibited several well-marked 3-D effects which are typical of shallow water environments. Some of them were already observed in the 3-D ASA wedge and 3-D Gaussian canyon test cases.

To conclude, let us make a comment on CPU times. It is well known that the main drawback of 3-D PE models is that they can be computationally expensive. For the sinusoidal test case studied in this paper, solving the pulse propagation problem using a fully 3-D calculation took approximately 14 days of CPU time whereas the 2-D calculation took approximately half an hour only. It should be noted that, as already mentioned, all the numerical simulations presented here were performed on a 2.8-GHz monoprocessor workstation with a 2-GB memory, and neither vectorization nor parallel computing was used. Recently, a parallel version of the code was developed and very good efficiency and reduction in CPU time were obtained on a massively parallel computer. For instance, the use of 64 processors in parallel allowed to solve a 4-D propagation benchmark problem (three-dimensional extension of the ASA wedge problem) in less than one hour. For comparison, solving the same problem by using only one single processor required approximately one day and a half of computation. Therefore, the use of such a parallel algorithm would certainly enable us to reduce significantly the CPU times (7 hours instead of 14 days) and hence allow the analysis of this 4-D acoustical problem at higher frequencies and/or longer propagation ranges.

References

[1] A. Tolstoy: 3D propagation issues and models. J. Comp. Acous. **4** (1996) 243–271.

[2] M. J. Buckingham: Theory of acoustic propagation around a conical seamount. J. Acoust. Soc. Am. **80** (1986) 265–277.

[3] C. H. Harrison: Three-dimensional ray paths in basins, troughs, and near seamounts by use of ray invariants. J. Acoust. Soc. Am. **62** (1977) 1382–1388.

[4] J. A. Fawcett: An efficient three-dimensional boundary integral equation method for solving azimuthally symmetric scattering problems in the oceanic waveguide. J. Acoust. Soc. Am. **94** (1993) 2307–2314.

[5] J. S. Papadakis, V. A. Dougalis, N. A. Kampanis, E. T. Flouri, B. Pelloni, A. Plaisant, E. Noutary, L. Bjørnø, P. Nielsen, D. Zhu: Ocean acoustic models for low frequency propagation in 2D and 3D environments. Acta Acustica united with Acustica **84** (1998) 1031–1041.

[6] C. H. Harrison: Acoustic shadow zones in the horizontal plane. J. Acoust. Soc. Am. **65** (1979) 56–61.

[7] H. Weinberg, R. Burridge: Horizontal ray-theory for ocean acoustics. J. Acoust. Soc. Am. **55** (1974) 63–79.

[8] M. J. Buckingham: Theory of three-dimensional acoustic propagation in a wedgelike ocean with a penetrable bottom. J. Acoust. Soc. Am. **82** (1987) 198–210.

[9] M. J. Buckingham, A. Tolstoy: An analytical solution for benchmarks problem 1: The "ideal" wedge. J. Acoust. Soc. Am. **87** (1990) 1511–1513.

[10] E. K. Westwood: Broadband modeling of the three-dimensional penetrable wedge. J. Acoust. Soc. Am. **92** (1992) 2212–2222.

[11] J. A. Fawcett: Modeling three-dimensional propagation in an oceanic wedge using parabolic equation methods. J. Acoust. Soc. Am. **93** (1993) 2627–2632.

[12] C. H. Harrison: Wave solutions in three-dimensional ocean environments. J. Acoust. Soc. Am. **93** (1993) 1826–1840.

[13] G. B. Deane, M. J. Buckingham: An analysis of the three-dimensional sound field in a penetrable wedge with a stratified fluid or elastic basement. J. Acoust. Soc. Am. **93** (1993) 1319–1328.

[14] K. B. Smith: A three-dimensional propagation algorithm using finite azimuthal aperture. J. Acoust. Soc. Am. **106** (1999) 3231–3239.

[15] F. Sturm, J. Fawcett: On the use of higher-order azimuthal schemes in 3-D PE modeling. J. Acoust. Soc. Am. **113** (2003) 3134–3145.

[16] A. Tolstoy, K. Smith, N. Maltsev: The SWAM'99 workshop - an overview. J. Comp. Acous. **9** (2001) 1–16.

[17] F. Sturm: Numerical study of broadband sound pulse propagation in three-dimensional oceanic waveguides. J. Acoust. Soc. Am. **117** (2005) 1058–1079.

[18] M. D. Collins, S. A. Chin-Bing: A three-dimensional parabolic equation model that includes the effects of rough boundaries. J. Acoust. Soc. Am. **87** (1990) 1104–1109.

[19] F. Sturm: Numerical simulations with 3DWAPE considering shallow water range-dependent environments. J. Acoust. Soc. Am. **109** (2001) 2334–2335.

[20] M. D. Collins: Higher order padé approximations for accurate and stable elastic parabolic equations with application to interface wave propagation. J. Acoust. Soc. Am. **89** (1991) 1050–1057.

[21] F. D. Tappert: The parabolic approximation method. – In: Wave propagation and underwater acoustics, Lecture notes in physics. J. Keller, J. Papadakis (eds.). Springer, Berlin, 1977, 224–287.